Surface & Coatings Technology 494 (2024) 131546

Contents lists available at ScienceDirect

Surface & Coatings Technology

journal homepage: www.elsevier.com/locate/surfcoat

Corrosion mechanisms of TiO_2 photoelectrode coatings in alkaline conditions

Lauri Palmolahti [a], Jussi Hämelahti [a], Markku Hannula [a], Harri Ali-Löytty [a,b,*], Mika Valden [a,*]

[a] Surface Science Laboratory, Physics Unit, Faculty of Engineering and Natural Sciences, Tampere University, Tampere, Finland
[b] Liquid Sun Ltd., Tampere, Finland

ARTICLE INFO

Keywords:
Thin films
Chemical stability
TiO_2
EIS
ALD

ABSTRACT

The crystal structure of TiO_2 has a significant impact on the chemical stability of the protective TiO_2 thin films used in photoelectrochemical conditions. By altering the deposition temperature of the atomic layer deposition method, and by post-deposition annealing treatments, amorphous, microcrystalline anatase, and Ti^{3+}-rich nanocrystalline rutile structures can be achieved. In this paper, the chemical stability in alkaline solution and failure mechanisms of ALD grown TiO_2 thin films on Si(100) were studied by SEM, XPS, EIS, and ellipsometry. The results showed that the electrically conductive Ti^{3+}-rich nanocrystalline rutile thin film was chemically stable, whereas other samples failed within the first 10 h of the test in 1.0 M NaOH. More detailed analysis in 0.1 M NaOH revealed that the anatase sample experienced sudden failure after NaOH solution penetrated the TiO_2 via grain boundaries, causing the Si substrate to dissolve. In contrast, the amorphous TiO_2 films had more gradual failure as the NaOH solution permeated the TiO_2 film, causing it to swell up to three times the initial thickness of the film.

1. Introduction

TiO_2 thin films are widely used as protective coatings in photocatalytic applications, such as photoelectrodes [1]. Thus, the chemical stability and protective properties of TiO_2 thin films with different crystal structures have been an intensively studied topic and are major targets of development [2,3]. The chemical stability impacts the durability of the material and the degradation of the molecular structure of the thin film may result in severe failure of the photoelectrode coating. Besides the amorphous phase, TiO_2 has three crystalline phases: anatase, rutile, and brookite [4], from which rutile is considered being the most chemically stable one [5]. TiO_2 thin films can also feature mixed phases [6] with varying crystallite sizes, which can affect the chemical stability [7,8]. Porosity and nanocrystallinity have gained great interest, because of their high photocatalytic efficiency [9,10]. Mesoporous amorphous TiO_2 nanostructures are especially interesting as they can be used as lithium-storage in batteries [11].

The reduction potential of TiO_2 is at higher energy compared to the conduction band [12]. For this reason, TiO_2 is not prone to reduction, as the valence band electrons do not have enough energy. However, the oxidation potential is above the valence band, which allows holes to cause oxidation. The O_2/H_2O oxidation potential is also above the valence band and thus these two oxidation reactions compete from the same electron holes. The oxidation of TiO_2 has slow reaction kinetics, making the water oxidation more favorable [13], which protects TiO_2 from anodic decomposition. The energy level for the hole mediated oxidation of TiO_2 is lower compared to the oxidation of water, which also promotes water being oxidized and not the TiO_2 [12].

TiO_2 is slightly soluble in alkaline electrolytes [14] and a higher concentration of alkalis, e.g. of NaOH, increases the degradation rate [5]. Under alkaline conditions that are used in photocatalytic applications, several mechanisms cause degradation of TiO_2. These mechanisms include hydroxylation, intercalation, and corrosion [13,15]. Hydroxylation is mediated by adsorption of hydroxyl groups onto the sample surface [13], whereas the entry of protons to the TiO_2 oxide lattice causes intercalation [13]. The degradation can affect the TiO_2 layer directly or it can affect the underlying substrate [16]. Especially, any non-uniform structures of the TiO_2 layer can enhance degradation [15]. Degradation can start from small defects [17] such as grain boundaries and can thus cause pinholes by localized corrosion [18]. Pinholes can also exist in amorphous TiO_2 films and exist more likely in thinner films [19]. The degradation at the grain boundaries can lead to a formation of

* Corresponding authors at: Surface Science Laboratory, Physics Unit, Faculty of Engineering and Natural Sciences, Tampere University, Tampere, Finland.
E-mail addresses: harri.ali-loytty@tuni.fi (H. Ali-Löytty), mika.valden@tuni.fi (M. Valden).

https://doi.org/10.1016/j.surfcoat.2024.131546
Received 25 July 2024; Received in revised form 5 November 2024; Accepted 8 November 2024
Available online 9 November 2024
0257-8972/© 2024 The Authors. Published by Elsevier B.V. This is an open access article under the CC BY license (http://creativecommons.org/licenses/by/4.0/).

channels that allow the electrolyte to penetrate through the TiO_2 overlayer into the TiO_2–substrate interface. If Si substrate is used, the electrolyte that has penetrated the TiO_2 layer causes degradation of the Si substrate, which results in formation of inverse pyramid shaped voids, which can lead to the failure of the protective coating [16]. Hence, it is essential to determine different failure mechanism of protective TiO_2 thin films in various electrolytes. Nanostructuring of TiO_2 can enhance the charge transfer properties of the TiO_2 thin film [20] and the increased surface area of patterned TiO_2 increases the photocatalytic efficiency of TiO_2, but also increases the mechanical stability and resistance to peeling [21]. While nanostructuring of TiO_2 may improve TiO_2 properties, it remains challenging to transfer the good properties to a photoelectrode protection layer.

TiO_2 thin films can be fabricated using various methods [22–24]. Atomic layer deposition (ALD) is a versatile method for growing conformal TiO_2 thin films [22]. The thickness and molecular structure of the ALD TiO_2 thin films can be precisely controlled, which makes ALD an excellent choice for photocatalytic applications [22]. It has been shown that under alkaline conditions, amorphous ALD TiO_2 films are not chemically as stable as crystalline phases [18,25–27]. However, post-deposition annealing treatments can be performed to enhance the chemical stability via crystallization [18,27]. The resulting polymorph and crystallite size can be selected by fine tuning the deposition parameters of amorphous TiO_2 [18,27]. The resulting crystal structure is thus predetermined by the properties of the amorphous phase.

In the present work, the failure mechanisms and chemical stability and the protective properties of ALD grown microcrystalline anatase, nanocrystalline rutile, and amorphous TiO_2 thin films were studied using 120 h stability tests in 0.1 and 1.0 M NaOH solutions. In this work, the microcrystalline anatase refers to an anatase thin film where the horizontal crystallite size is between 0.1 and 100 μm although the thickness of the film is below the micrometer range. A thickness of 30 nm was selected as it can serve as an anti-reflection coating [28] while allowing good charge transfer properties across the film when applied as a photoelectrode coating [1]. The impedance response and open circuit potential (OCP) were monitored during the chemical stability tests and the thickness, porosity, and structure of the films were analyzed by X-ray photoelectron spectroscopy (XPS), ellipsometry and scanning electron microscopy (SEM). Results showed that the nanocrystalline rutile protected the substrate, whereas amorphous and microcrystalline anatase did not. Amorphous TiO_2 swelled up to 3 times the initial thickness of the film and formed a porous structure. Porous structure allowed the electrolyte to permeate through the film. The microcrystalline anatase featured long grain boundaries that also allowed the electrolyte to penetrate to the substrate–TiO_2 interface.

2. Experimental

2.1. Sample fabrication

TiO_2 thin films were fabricated by ALD on prepolished n-type Si(100) wafer (Siegert Wafer, Sb doped). The deposition was carried out in Picosun Sunale R-200 Advanced ALD reactor. Before starting the deposition, the substrates were held in the reaction chamber for 30 min to stabilize the temperature. Tetrakis(dimethylamido)titanium(IV) (electronic grade 99.999+%, Sigma-Aldrich) and ultrapure Milli-Q water were used as precursors. During the deposition, TDMAT bubbler and the precursor gas delivery line were kept at 76 and 85 °C, respectively, to reach the proper vapor pressure and to prevent condensation of the precursor. The water was cooled to 18 °C with a Peltier element. Ar gas was used as a carrier/purge/venting gas (99.9999 %, Oy Linde Gas Ab). The continuous Ar flow in the TDMAT and water lines was 100 sccm. The deposition was started with a 1.6 s TDMAT pulse and was followed by a 0.1 s water pulse. Between each pulse, the excess precursor was flushed during a 6.0 s purge period. The targeted thickness of 30 nm was achieved by repeating a predetermined number of precursor pulses (cycles). Two sets of samples were fabricated using 100 and 200 °C deposition temperatures. To achieve the 30 nm film thickness, 480 and 870 growth cycles were used for 100 and 200 °C deposition temperatures, respectively.

After the deposition, a part of the samples was annealed in ultra-high vacuum at 500 °C in the preparation chamber of NanoESCA spectromicroscopy system (Omicron NanoTechnology GmbH). The temperature was monitored using a pyrometer (Land Cyclops 160B). Emissivity of 0.60 was used. The temperature was increased from room temperature to 500 °C over a 0.5 h period and then the temperature was kept constant for 1 h. Samples were allowed to cool back to room temperature before removing from the preparation chamber. Total of four different samples were fabricated labeled as TiO_2(100 °C) as dep., TiO_2(200 °C) as dep., TiO_2(100 °C) ann., and TiO_2(200 °C) ann., where the temperature in the parentheses denotes the deposition temperature. The as dep. denotes no annealing treatment and ann. denotes 500 °C post deposition annealing in vacuum.

2.2. Sample characterization

The fabricated samples were characterized before and after the stability tests by SEM, XPS, and ellipsometry. SEM images were taken by InLens detector of Zeiss Ultra-55 microscope. XPS was measured using non-monochromatized Al Kα radiation ($h\nu = 1486.6$ eV, V. G. Microtech, 8025 twin anode X-ray source). The kinetic energy and electron intensity of the photoelectrons were measured using hemispherical energy analyzer and electron detector (V. G. Microtech, CLAM4MCD LNo5). The pass energy of the analyzer was 20 eV for the detail scans and 50 eV for the survey scans. The pressure of the XPS system was below 2×10^{-8} mbar. The measured spectra were analyzed using CasaXPS (Version 2.3.25PR1.0) software [29]. Shirley-type background subtraction was used. Thickness and refractive index of the samples was measured by an ellipsometer (Rudolph AutoEL III) using a 632.8 nm He—Ne laser and a laser angle of 70 degrees. Refractive index of 3.863 [30] and extinction coefficient of 0.162 were used for the Si substrate [31].

2.3. Stability tests and electrochemical measurements

Chemical stability tests were performed in a custom made electrochemical cell, where a circular area of the sample with a diameter of 6 mm was in contact with the electrolyte. The electrolytes were 0.1 and 1.0 M air-saturated NaOH solutions (Baker analyzed J.T. Baker) without forced convection, and the amount of dissolved oxygen was controlled by maintaining an open-air contact to the electrolyte. The volume of the electrolyte was 3.5 ml. If the whole TiO_2 thin film would be dissolved into the electrolyte, the concentration of TiO_2 would be 13 μmol/l. This amount is insignificant and thus the consumption of OH groups due to the dissolution process is also negligible. During the stability test, open circuit potential (OCP) and electrochemical impedance spectroscopy (EIS) were measured. These measurements were conducted using a three electrode setup, where platinum wire was used as a counter electrode, Ag/AgCl-electrode as a reference electrode (Harvard Apparatus, Leak-Free reference electrode 69–0023), and the sample as a working electrode. Measurements were done using potentiostat/galvanostat (Autolab PGSTAT204, Metrohm AG). EIS was measured using galvanostatic mode. The DC component of the current was 0 and the AC component was 0.01 mA. Frequency range from 0.1 Hz to 1 MHz was measured. EIS and OCP measurements were repeated every 15 min during the stability tests. The measured OCP values were converted to potential versus standard hydrogen electrode (SHE) using the equation $V_{SHE} = V_{Ag/AgCl} + 0.197$ V. All the stability tests were performed at the open circuit potential, i.e., without any bias potential or photoinduced charge transfer, and reflect chemical stability of samples in NaOH. AC amplitude of the EIS measurement was the same for all the samples and was assumed to play no role to the corrosion mechanism.

3. Results

3.1. Structure and composition

The effect of the 120 h stability tests in 0.1 and 1.0 M NaOH was studied by SEM, (Fig. 1), and XPS (Fig. 2). Before the stability tests, the SEM images showed that the as deposited TiO_2 samples did not feature any structure, that is characteristic of the amorphous phase. In contrast, the TiO_2(100 °C) ann. sample showed large fern leaf-like patterns indicating microscale crystallite size, whereas the TiO_2(200 °C) ann. sample showed a nano-scale structure. The same set of samples were characterized in our earlier research by a combination of SEM, grazing incidence x-ray diffraction, and near edge X-ray absorption fine structure spectroscopy [18]. Those results showed that the as deposited samples are amorphous, and the 100 °C and 200 °C deposited samples crystallize to microcrystalline anatase and nanocrystalline rutile, respectively, upon annealing at 500 °C. Samples deposited at 200 °C have more Ti^{3+} defects [18]. Crystallization also increases the amount of Ti^{3+} defects, and thus the nanocrystalline rutile is the most Ti^{3+}-rich of the samples [18].

After the 120 h stability test in 0.1 M NaOH, the amorphous as deposited samples show holes in the structure. This is contrary to the crystalline samples.

By comparing the structure of the amorphous TiO_2 after stability test in 0.1 M NaOH to SEM images presented in literature [32], the structure was identified to be mesoporous with an estimated pore size of roughly 30 nm. The pore size is similar to the thickness of the film. The visual inspection of TiO_2(100 °C) as dep. sample showed no signs of changes, whereas the visual inspection of TiO_2(200 °C) as dep. sample showed that the TiO_2 film had begun to flake off at the edges. Metallic Ti has been reported to result in a similar mesoporous structure by anodic oxidation of TiH_2 species when immersed into NaOH solution [33]. Ti—H species are also reported to be formed on the TiO_2 surface [34], which means that the mesoporous TiO_2 can be formed with similar process.

The SEM image and visual inspection of the anatase TiO_2(100 °C) ann. sample showed that the TiO_2 film had flaked off completely, exposing the Si substrate. This indicates that microcrystalline anatase thin film does not protect Si(100) substrate in 0.1 M NaOH solution, which was expected as ALD anatase has been reported to suffer from grain boundary mediated corrosion [18,27]. In contrast, the rutile TiO_2(200 °C) ann. sample did not show signs of failure, although the SEM images showed a difference in the surface structure after the stability tests. This shows that the TiO_2(200 °C) ann. is stable and protects the substrate in 0.1 M NaOH, which is also supported by our earlier measurements [18].

The 1.0 M NaOH is much more corrosive compared to 0.1 M. SEM images and visual inspection show that all samples except TiO_2(200 °C) ann. flaked off completely during the 120 h stability test in 1.0 M NaOH. This suggest that the amorphous TiO_2 and microcrystalline anatase do not protect the Si substrate in 1.0 M NaOH. On the other hand, based on the SEM images and visual inspection of the nanocrystalline rutile TiO_2(200 °C) ann. sample, there were not any significant differences between samples tested in 0.1 and 1.0 M NaOH, which indicates that the sample is in a stable state. The surface of the TiO_2(200 °C) ann. sample featured flakes after the stability tests. We interpret these flakes to be

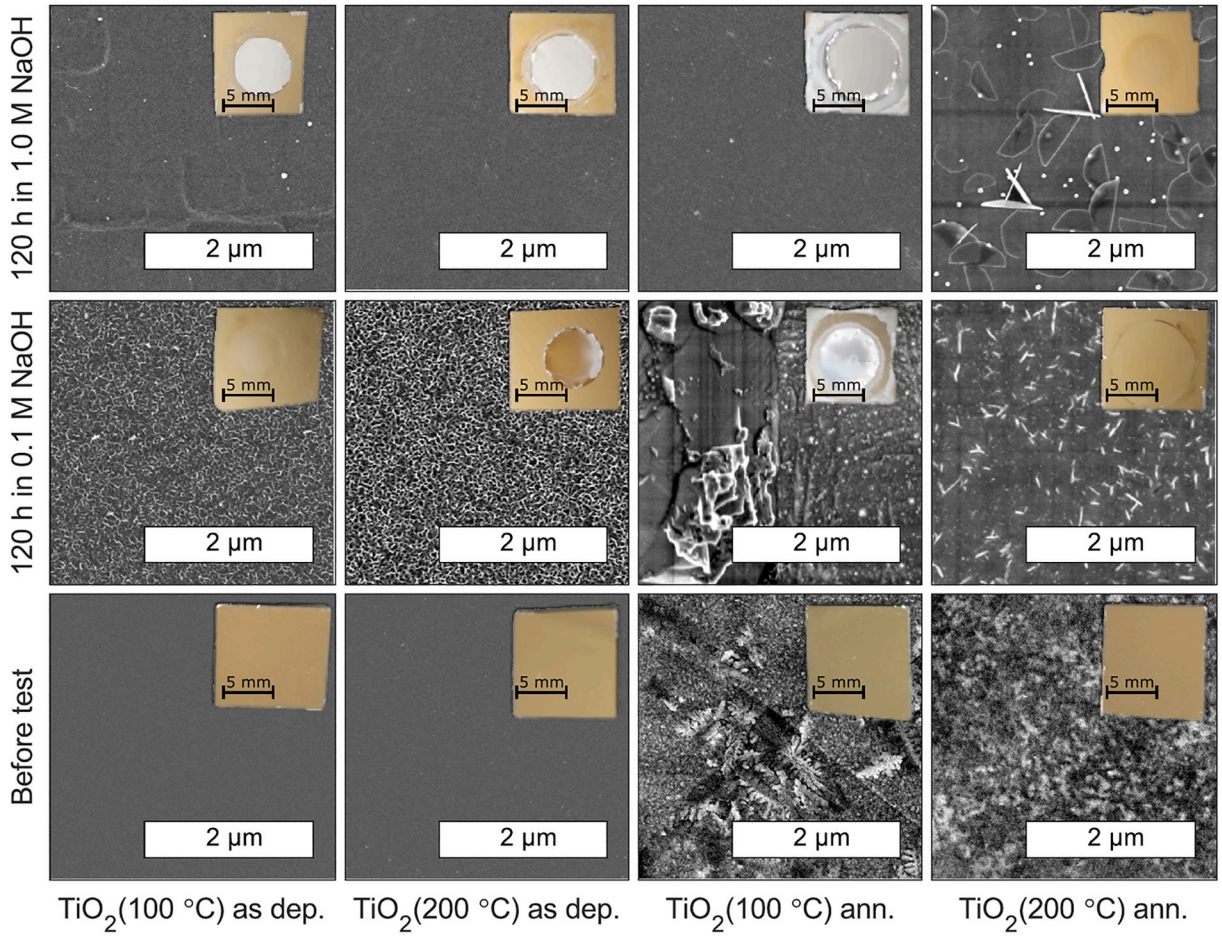

Fig. 1. SEM images of the samples before the stability tests and after the 120 h stability tests in 0.1 and 1.0 M NaOH. Results of the visual inspection of the samples are presented as insets. SEM images were taken from the middle of the samples.

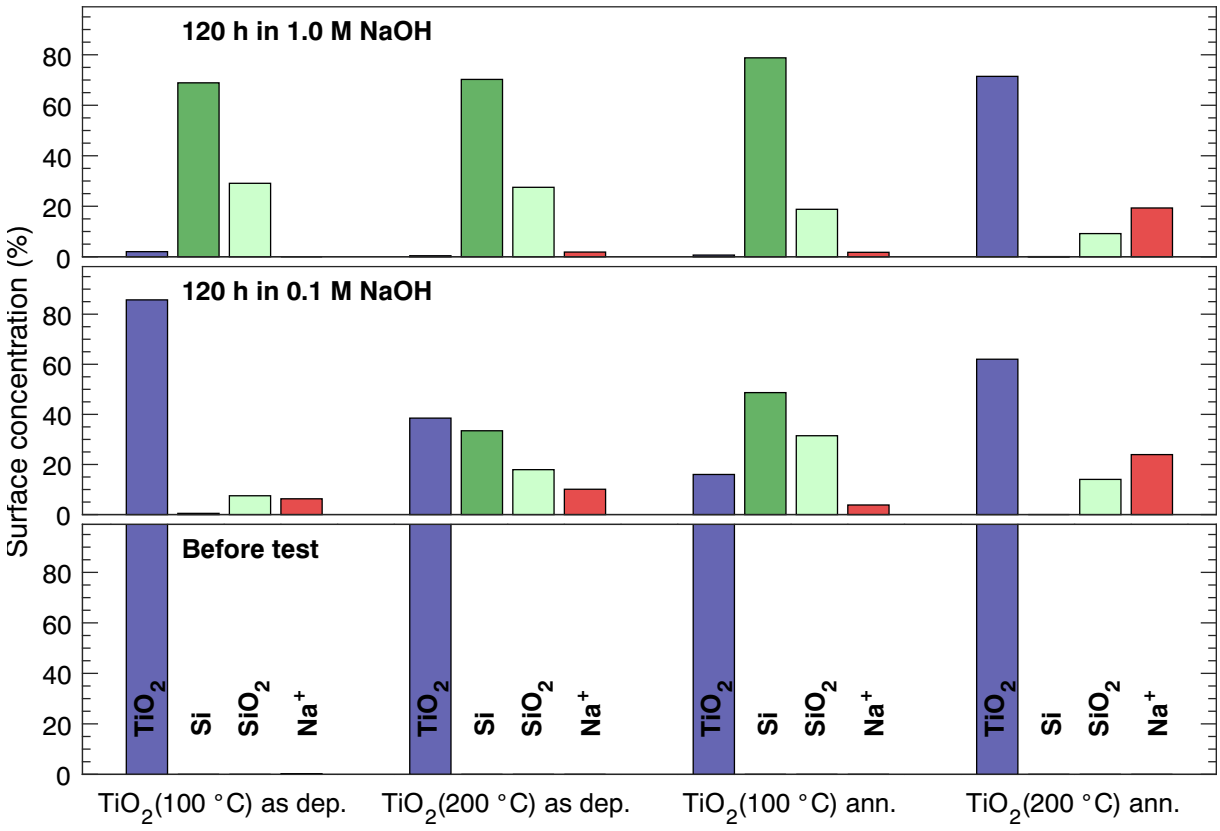

Fig. 2. Surface composition of the samples measured with XPS before the stability tests and after the 120 h stability tests in 0.1 and 1.0 M NaOH.

NaOH as similar flakes have been reported to be formed from other hydroxides [35]. This interpretation is also supported by the higher Na content, presented later in the XPS results.

To support the results obtained from the SEM images and visual inspection, the surface composition of the samples was analyzed by XPS before and after the 120 h stability tests. Ti, O, Si, Na, and C were identified from the survey spectra (Fig. S1). XPS is very surface sensitive method, and thus even very small quantities of surface impurities are visible in the spectra [36]. The amounts of four different compounds, TiO_2, Si, SiO_2, and Na^+, were analyzed from the high resolution XPS spectra and are shown in Fig. 2 [25,37]. The concentrations of different compounds were calculated from the peak areas presented in Fig. S2. The concentration of compounds was fitted so that the modeled peak areas of different chemical components would match the measured peak areas by using least squares fitting method and relative sensitivity factors [38]. C is impurity resulting from atmospheric contamination and because O 1s peak did not feature significant contribution from C—O compounds, C was excluded from the analysis.

XPS results (Fig. 2) show that before the stability tests, the surface of the samples is TiO_2 as expected. After the 120 h stability test in 0.1 M NaOH, TiO_2(100 °C) as dep. sample did not have significant changes, whereas TiO_2(200 °C) as dep. sample had significantly less TiO_2 and more Si and SiO_2. This supports the interpretation that the film in TiO_2(200 °C) as dep. sample has begun to flake off. After 120 h in 0.1 M NaOH, the surface of the TiO_2(100 °C) ann. sample had only 16 % of TiO_2 left and had a significant amount of Si and SiO_2, indicating that most of the film has detached from the Si substrate. On the other hand, TiO_2(200 °C) ann. sample showed decreased amount of TiO_2 but did not show any elemental Si, that should be visible if the TiO_2 film has failed, supporting the interpretation that the film is intact. All samples showed varying amounts of Na^+ and SiO_2 after the stability tests. NaOH dissolves Si and SiO_2 [39] and thus if the electrolyte gets in contact with the Si substrate, Si and SiO_2 can be dissolved into the electrolyte and be migrated to the sample surface.

Only TiO_2(200 °C) ann. sample survived the 120 h stability test in 1.0 M NaOH and had TiO_2 remaining on the surface. The TiO_2(200 °C) ann. sample did not have any significant changes compared to the test in 0.1 M NaOH, which suggest that it is chemically stable. SEM, visual inspection, and XPS results all support each other in the conclusion that amorphous TiO_2 is unstable in NaOH solution and forms a porous structure and/or disintegrates depending on the exposure to NaOH. Microcrystalline anatase does not protect the substrate, whereas the nanocrystalline rutile does.

3.2. *Electrochemical measurements during the stability tests*

The porous structure of the amorphous samples or the holes at the grain boundaries of the anatase sample may allow NaOH solution to permeate to the TiO_2/Si interface [18,40]. In order to have more detailed information about the failure mechanism of the thin films, the changes in the samples during the stability tests were monitored with electrochemical measurements. The results of the OCP measurements during the stability tests in 0.1 M and 1.0 M NaOH are shown in Fig. 3. In 1.0 M NaOH, changes in OCP value take place within the first 10 h. There are at least two different phenomena that contribute to the change. Firstly, the surface of the sample stabilizes followed by the TiO_2–electrolyte interface reaching a steady state. Secondly, there are actual changes in the TiO_2 thin film. In 1.0 M NaOH, both phenomena occur so rapidly that it is difficult to distinguish them based on the OCP value. The SEM and XPS results show that TiO_2(200 °C) ann. is the only sample that does not feature changes during the stability tests. Thus, the change in the OCP value of the TiO_2(200 °C) ann. sample in 1.0 M NaOH from −0.4 to −0.7 V vs SHE can be assigned to the above-mentioned reaching of the steady state. The other samples show a further decrease to −1.1 V vs SHE, that are at least partially related to the failure of the TiO_2 films.

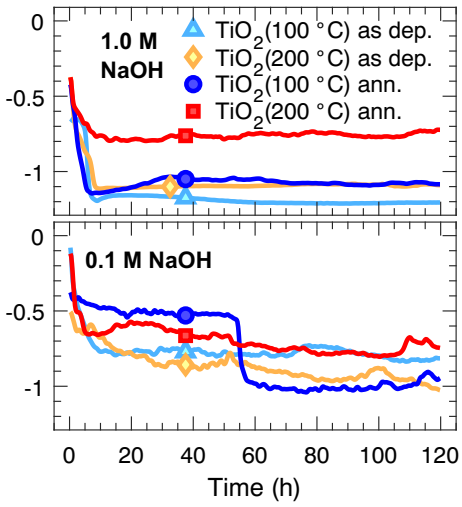

Fig. 3. OCP of the samples during the 120 h stability tests in 0.1 and 1.0 M NaOH.

In 0.1 M NaOH, changes in the TiO_2 film are slower, which is expected as the degradation of TiO_2 is more prominent in solutions with higher NaOH concentrations [5]. The initial decrease of the OCP value within the first 5 h of the stability test can be attributed to the surface stabilization. After 10 h, the OCP values are quite stable with one exception. The TiO_2(100 °C) ann. sample experiences a rapid decrease in the OCP value at 55 h into the stability test. This sudden change is induced by the failure of the anatase film that lets the electrolyte to get in contact with the Si substrate. This clearly indicates that the failure mechanism is different compared to the amorphous samples.

To obtain a better understanding of the failure mechanism, EIS measurements were performed during the stability tests. The impedance data was fitted with an equivalent circuit that is presented in Fig. 4. The circuit consists of three parallel connections of resistor (R) and capacitor (C) or resistor and constant phase element (Q,CPE). The first (leftmost) resistor–constant phase element pair represents the sample–electrolyte interface, the second TiO_2–Si interface, and the third pair represent the impedance response of the measurement setup, that includes electrolyte resistance and the capacitance of the counterelectrode–electrolyte and Si–ohmic-contact interfaces. The Nyquist plots of the measured and fitted data are presented in the Supplementary Video 1. The Nyquist plots show that the equivalent circuit models the measured data precisely. All data from all samples were fitted using the same equivalent circuit to make the comparison between different samples and cases more reliable. Based on the preliminary fittings, the exponent of Q_3 CPE was set to a fixed value of 0.75 and the resistance of R_1 to 30 kΩ as these values did not feature any consistent changes. Fixing these two values reduced the randomness in the fit without losing any significant information, thus improving the overall quality of the fit. The capacitance (Q_1) and the exponent (n_1) of the CPE describing the TiO_2–electrolyte interface and the capacitance (C_2) of the capacitor describing the TiO_2–Si interface were selected for more detailed analysis and are presented in Fig. 4. The first 2 h of the stability tests were excluded from Fig. 4 as the changes in the samples were so fast that the impedance of the sample changed significantly during a single EIS measurement, making the fitting unreliable.

CPEs are required in the equivalent circuit to model the non-ideal capacitance of the interfaces caused by the inhomogeneities at the interface [41]. The exponent of a CPE describing an ideal capacitor is 1, but surface roughness and porosity cause the capacitance of the interface to be unideal and thus decrease the exponent of a CPE to have a value less than one [41]. The amorphous TiO_2 samples had low n_1 values due to the high surface roughness and/or porosity. When this information is combined with the results obtained from the SEM images, the low n_1 value can be assigned to the porosity of the TiO_2 thin film. Fig. 4 shows that the n_1 of amorphous samples is below 0.8 already at the first EIS data point at 2 h of the stability test, suggesting that the surface becomes rough and/or porous within the first 2 h of the stability test.

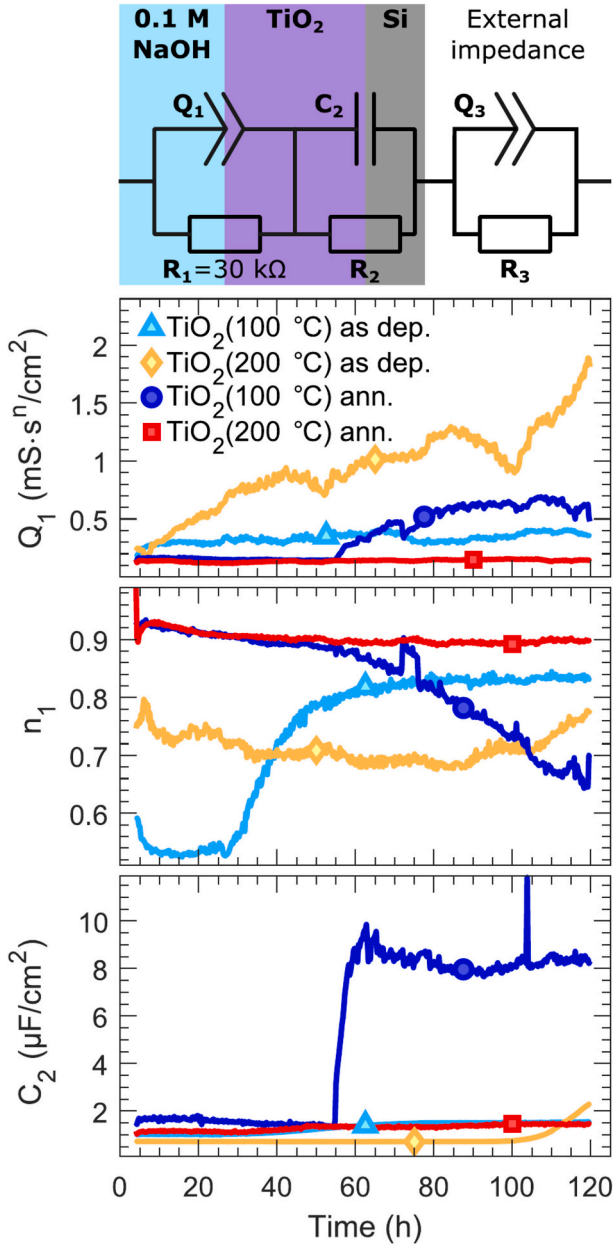

Fig. 4. Selected components of the equivalent circuit (shown on top) fitted to the electrochemical impedance data collected during the 120 h stability test in 0.1 M NaOH. Values of all components are presented in Fig. S3.

The surface area of the TiO_2–electrolyte interface of porous films is larger compared to solid films [42]. However, the capacitance of the interface does not scale linearly with the increased surface area due to porosity [42], because the pores are too small to contribute to the double-layer capacitance [43]. The amorphous as deposited samples show a gradual increase in Q_1 capacitance, which indicates gradual change. The C_2 capacitance of the TiO_2–Si interface is almost constant for the amorphous samples, suggesting that the TiO_2 film is intact. However, TiO_2(200 °C) as dep. sample has a subtle change in the C_2 capacitance after 100 h of the stability test, indicating a change in the TiO_2–Si interface. This change is also visible in n_1 and Q_1 values. As the XPS data and visual inspection of TiO_2(200 °C) as dep. sample also

showed signs of onset of failure, this feature in the EIS model can be interpreted as a breach of electrolyte through the TiO_2 film onto the Si substrate.

The behavior of the crystalline samples was different. As expected, based on the XPS, SEM, visual inspection, and OCP results, the TiO_2(200 °C) ann. sample was stable and did not have any significant changes in the EIS response. As anticipated by the OCP measurements, the TiO_2(100 °C) ann. sample was stable up to 55 h. After that there was a rapid step like change in the C_2 capacitance, indicating that the electrolyte breached through the TiO_2 film and contacted the Si substrate. Also, the n_1 value started to decrease and the Q_1 increase at that instant. This can be interpreted as an increase in surface roughness that would be expected if there is grain boundary mediated corrosion. The hypothesis of the grain boundary mediated corrosion is further supported by atomic force microscopy images, that show intergranular corrosion of microcrystalline anatase thin films after similar stability tests [18].

Electric charge can be transferred from the TiO_2 into the electrolyte via different paths. In the porous material, the charge can be transferred via the TiO_2 onto the top surface of the film, where it is transferred into the electrolyte. The other route is that the charge is transferred from the TiO_2 into the electrolyte in the pores of the thin film, from where it is transferred forward along the pores [44]. If the charge transfer is dominated by the former case, the ion concentration inside the pores or the pore geometry will not affect the charge transfer resistance. The TiO_2–electrolyte interface was successfully modeled by a parallel resistor–CPE pair, where the resistor had a constant resistance of 30 kΩ. This supports the case where the charge is transferred from the top surface of the thin film into the electrolyte. The electrical conductivity of the TiO_2 thin films increases with the increased Ti^{3+} defect concentration because of polaron hopping [45]. The nanocrystalline TiO_2 has the largest concentration of Ti^{3+} defects [18], and thus has the highest electrical conductivity. However, the charge transfer is not limited by the bulk conductivity and the chemical stability does not depend on the bulk conductivity.

3.3. Swelling and failure mechanism

To investigate the changes in the film thickness during the stability test, ellipsometry measurements were performed for the amorphous as deposited samples. The measurements were conducted after shorter stability tests, conducted with separate samples. The durations of the stability tests were selected based on the changes in the impedance response. The obtained thicknesses and refractive indices are shown in Fig. 5. In 0.1 M NaOH, the thickness of both films gradually increases during the stability test. In 1.0 M NaOH, the change is much faster and more intense. The thickness of both samples decreases to zero between 7 and 10 h, indicating disintegration of the TiO_2 thin film. This is consistent with the OCP measurement that also showed signs of the failure within the first 10 h. The refractive index of TiO_2 depends slightly on the density of TiO_2 [46]. TiO_2 with densities ranging from 2.4 to 3.1 g/cm^3 has refractive indices from 2.0 to 2.3 [46]. The refractive indices of 2.33 and 2.16 measured before the stability tests for the TiO_2(100 °C) as dep. and TiO_2(200 °C) as dep. samples, respectively, are similar to these literature values.

Based on the data presented in Fig. 5, the refractive index seems to decrease when the thickness increases. The refractive indices were studied as a function of the porosity of the samples. The hypothesis is that the amount of TiO_2 does not change during the swelling phase of the stability test and that empty voids are formed inside the TiO_2. The refractive indices of two mixed phases, in this case TiO_2 and air, can be modeled using the equation

$$n^2 = \phi n_{\text{air}}^2 + (1-\phi) n_{\text{TiO}_2}^2 \quad (1)$$

where ϕ is the porosity of the material [47]. The refractive index of air is 1. The porosity can be calculated by $\phi = d_0/d$, where d_0 is the initial

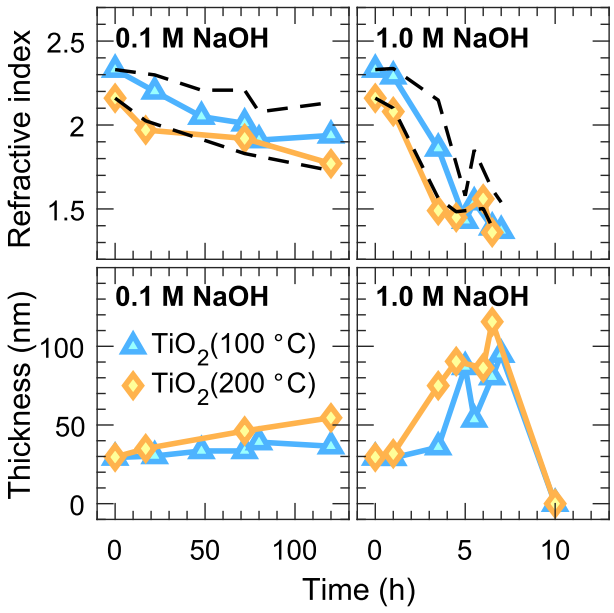

Fig. 5. Thickness and refractive index at 632.8 nm wavelength of the as deposited samples during the stability tests in 0.1 and 1.0 M NaOH. The dashed black line is the theoretical refractive index calculated using eq. 1.

thickness of the film and d is the measured thickness at any given time of the stability test. The modeled refractive index is shown as dashed lines in the Fig. 5. The model corresponds to the measured value well, which supports the formation of a porous film. It is possible that the electrolyte could stay inside the porous structure. However, if the refractive index of water ($n_{\text{air}} = 1.35$ [48]) is used instead of air, the values given by the eq. 1 are much less coincident with the experimental results. This indicates that the electrolyte does not stay inside the porous TiO_2 after the stability tests. No differences in swelling as a function of Na^+ content was observed between the amorphous samples deposited at different temperatures.

More detailed SEM images were used to confirm the interpretations of the failure mechanism of amorphous TiO_2 thin films in NaOH solution. The left column of Fig. 6 shows TiO_2(200 °C) as dep. sample after 6 h in 1.0 M NaOH. This instance is a focus of interest as the TiO_2 thin film is near to its maximum thickness. The right column shows the TiO_2(200 °C) as dep. sample after 120 h in 0.1 M NaOH, when the sample was at the beginning of disintegration. The cross-sectional view of the TiO_2(200 °C) as dep. sample after 6 h in 1.0 M NaOH shows that the TiO_2 film has swollen to almost three times the initial thickness. This corresponds well with the thickness measured with ellipsometry. The cross-sectional view clearly shows the porosity of the TiO_2 film. Even though the electrolyte has permeated through the film onto the Si substrate, the film is still attached to the substrate. The permeated electrolyte dissolves Si and causes the formation of inverse pyramids [16]. The geometry of these inverse pyramids conforms the crystalline planes of the single crystalline Si [49].

The right column of Fig. 6 shows the TiO_2(200 °C) as dep. sample after 120 h in 0.1 M NaOH, when the disintegration of the TiO_2 thin films is starting to take place. The inverse pyramids under the TiO_2 film are several micrometers in size. Thus, the unsupported length of the TiO_2 overlayer film is hundreds of times larger than the film thickness, resulting in a failure of the TiO_2 film. The top-down images show no signs of failure until the TiO_2 film starts to flake off. There is no difference in the nanoscale structure or in the porosity of the TiO_2 film before and after the initial failure.

XPS results in Fig. 2 showed that there are significant changes in the Na^+ surface concentration depending on whether the TiO_2 is swollen or not, or if the TiO_2 film has flaked off. The flaked off samples showed only

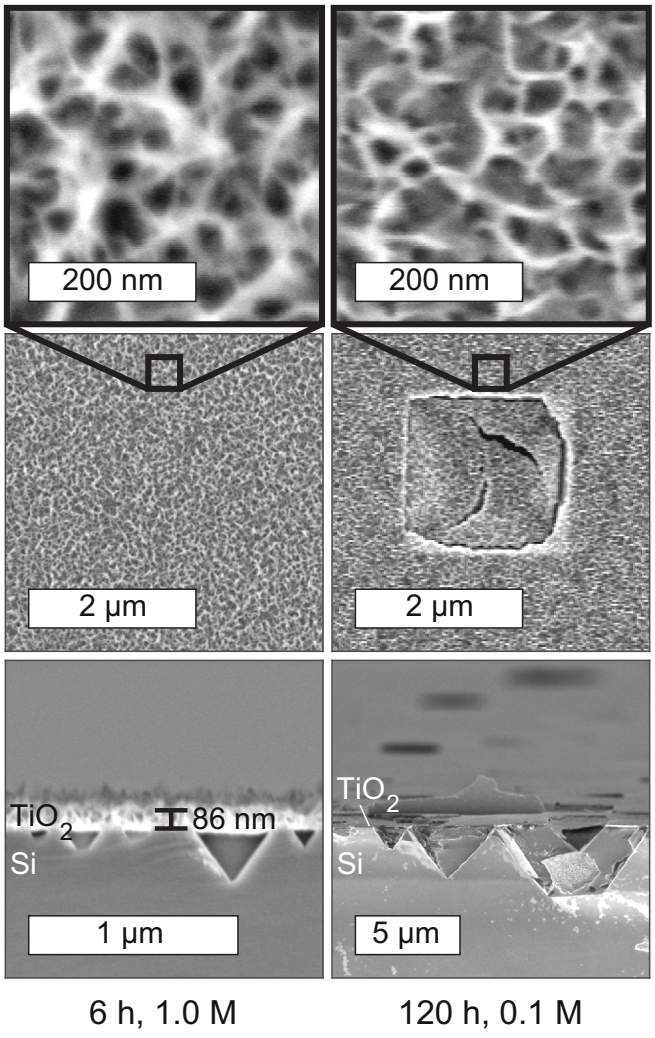

Fig. 6. SEM images of the TiO_2(200 °C) as dep. sample after 120 h stability test in 0.1 M NaOH and after 6 h stability test in 1.0 M NaOH. Cross-sectional images are shown in the bottom row.

negligible amount of Na^+. The relation between the Na^+ surface concentration and swelling of the films was studied further by measuring Na^+ concentration by XPS for selected points in Fig. 5. The obtained results are presented in Fig. 7, where the swelling factor, that is the measured thickness of the amorphous TiO_2 film relative to its initial thickness, is plotted as a function of the Na^+ surface concentration

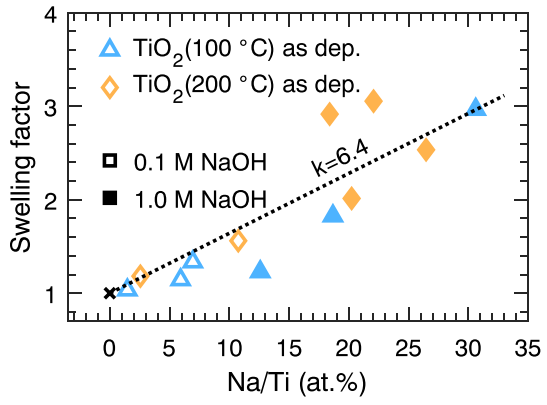

Fig. 7. The swelling factor of the amorphous TiO_2 thin films as a function of surface Na content during the stability tests.

relative to the amount of Ti. No change in the chemical state of Ti (Ti^{4+}) was observed for the swollen TiO_2 films. Also, it was not possible to identify any change in O 1s that could have indicated hydroxylation of TiO_2.

Fig. 7 shows that the swelling factor correlates strongly with the Na^+ content. It is concluded that Na^+ incorporates into the TiO_2 in the swelling process. Neither the electrolyte concentration nor the deposition temperature of amorphous TiO_2 have a significant effect on the relation between swelling factor and the Na^+ content. The linear fitting shows that the relationship between the two is linear and, for every 1 % increase in Na^+/Ti ratio, the film thickness increases by 6.4 % of the initial thickness. This approximation is valid at least up to a swelling factor of 3, at which point the thickness of the film has increased by 200 %.

4. Conclusions

In this research, the chemical stability and protective properties of amorphous, anatase, and rutile TiO_2 thin films on Si(100) in aqueous NaOH solution were studied. The amorphous thin films were deposited using ALD and the crystalline samples were fabricated by annealing the amorphous thin films in vacuum at 500 °C. The amorphous films were deposited at two different temperatures. The films deposited at 100 and 200 °C crystallize to microcrystalline anatase and nanocrystalline rutile, respectively. The results showed that the nanocrystalline rutile sample was chemically stable and protected the substrate up to 120 h in 0.1 and 1.0 M NaOH solutions. In contrast, the amorphous and microcrystalline anatase films did not protect the substrate and deteriorated within the first 10 h of the stability test in 1.0 M NaOH. The schematic presentation of the failure mechanisms of the TiO_2 thin films is presented in Fig. 8. The failure mechanism of amorphous TiO_2 and microcrystalline anatase were different. No significant differences in the stability were observed between the two amorphous TiO_2 samples deposited at 100 and 200 °C. Amorphous TiO_2 thin films became porous during the stability test and exhibited swelling up to three times the initial thickness before disintegration. Disintegration was affected by electrolyte permeating through the porous TiO_2 into the TiO_2–Si interface, where it caused dissolution of Si substrate. The dissolution of Si caused formation of inverse pyramid shaped voids in the Si surface, which eventually resulted in the detaching of the TiO_2 film from the substrate. The initial phase of the failure mechanism of the microcrystalline anatase was different. The anatase thin film did not show any signs of disintegration until 55 h into

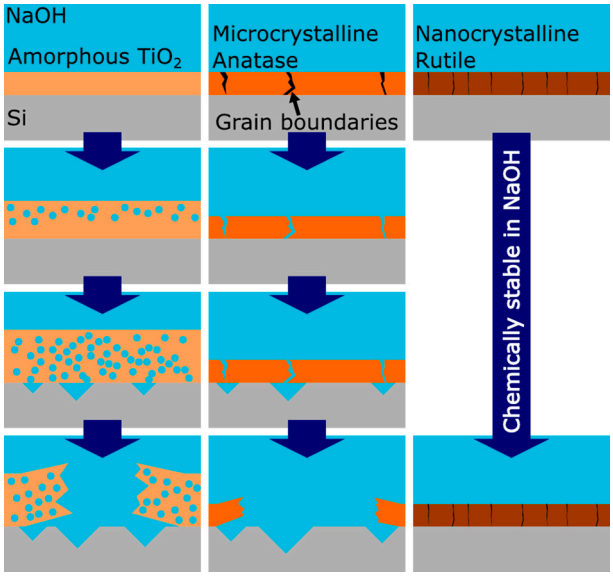

Fig. 8. Failure mechanisms of TiO_2 thin films in NaOH solution.

the stability test in 1.0 M NaOH, after which it exhibited a sudden change in impedance response and in OCP value. This rapid change was assigned to the electrolyte penetrating through the long grain boundaries of microcrystalline film into the TiO_2–Si interface. As with the amorphous samples, this caused dissolution of Si and the formation of inverse pyramid shaped voids, and finally the breakdown of the overlaying thin film. The nanocrystalline rutile did not feature such long grain boundaries as the microcrystalline anatase, making it resistant to grain boundary mediated corrosion. The chemical stability and protective properties combined with the good charge transfer properties of the defect rich nanocrystalline rutile make it a viable choice to be used as a protective coating in photoelectrodes.

CRediT authorship contribution statement

Lauri Palmolahti: Writing – original draft, Visualization, Supervision, Software, Formal analysis, Conceptualization. **Jussi Hämelahti:** Visualization, Investigation, Formal analysis, Conceptualization. **Markku Hannula:** Writing – review & editing, Conceptualization. **Harri Ali-Löytty:** Writing – review & editing, Supervision, Conceptualization. **Mika Valden:** Writing – review & editing, Supervision.

Declaration of competing interest

The authors declare that they have no known competing financial interests or personal relationships that could have appeared to influence the work reported in this paper.

Acknowledgments

This work was supported by the Academy of Finland (Decision No. 326461), the Jane & Aatos Erkko Foundation (project ”SOFUS”), and Business Finland (Decision No. 1464/31/2019). L.P. was supported by the KAUTE Foundation, Finnish Cultural Foundation, Vilho, Yrjö and Kalle Väisälä Foundation of the Finnish Academy of Science and Letters, and Emil Aaltonen Foundation. H.A.L. was supported by the Jenny and Antti Wihuri Foundation. This work is part of the Academy of Finland Flagship Programme, Photonics Research and Innovation (PREIN) (Decision No. 320165).

Appendix A. Supplementary data

Supplementary data to this article can be found online at https://doi.org/10.1016/j.surfcoat.2024.131546.

Data availability

The data supporting the findings of this study are available within the article and its supplementary materials.

References

[1] K. Sivula, Defects give new life to an old material: electronically leaky titania as a photoanode protection layer, ChemCatChem 6 (10) (2014).
[2] P.J. Reed, H. Mehrabi, Z.G. Schichtl, R.H. Coridan, Enhanced electrochemical stability of TiO_2-protected, Al-doped ZnO transparent conducting oxide synthesized by atomic layer deposition, ACS Appl. Mater. Interfaces 10 (50) (2018) 43691–43698.
[3] K. Bourikas, C. Kordulis, A. Lycourghiotis, Titanium dioxide (anatase and rutile): surface chemistry, liquid–solid interface chemistry, and scientific synthesis of supported catalysts, Chem. Rev. 114 (19) (2014) 9754–9823.
[4] D.A. Hanaor, C.C. Sorrell, Review of the anatase to rutile phase transformation, J. Mater. Sci. 46 (4) (2011) 855–874.
[5] E.V. Shkol'nikov, Thermodynamics of the dissolution of amorphous and polymorphic TiO_2 modifications in acid and alkaline media, Russ. J. Phys. Chem. A 90 (2016) 567–571.
[6] J. Kang, Y. Zhang, Z. Chai, X. Qiu, X. Cao, P. Zhang, G. Teobaldi, L.-M. Liu, L. Guo, Amorphous domains in black titanium dioxide, Adv. Mater. 33 (23) (2021) 2100407.
[7] T. Liu, F. Zhang, C. Xue, L. Li, Y. Yin, Structure stability and corrosion resistance of nano-TiO_2 coatings on aluminum in seawater by a vacuum dip-coating method, Surf. Coat. Technol. 205 (7) (2010) 2335–2339.
[8] H. Uzal, A. Döner, Corrosion behavior of titanium dioxide nanotubes in alkaline solution, Prot. Met. Phys. Chem. Surf. 56 (2) (2020) 311–319.
[9] C. Kang, L. Jing, T. Guo, H. Cui, J. Zhou, H. Fu, Mesoporous SiO_2modified nanocrystalline TiO_2 with high anatase thermal stability and large surface area as efficient photocatalyst, J. Phys. Chem. C 113 (3) (2009) 1006–1013.
[10] C.-C. Tsai, J.-N. Nian, H. Teng, Mesoporous nanotube aggregates obtained from hydrothermally treating TiO_2 with NaOH, Appl. Surf. Sci. 253 (4) (2006) 1898–1902.
[11] Y. Liu, C. Ding, X. Yan, P. Xie, B. Xu, L. Chen, Y. Liu, C. Liu, Y. Yu, Y. Lin, Interface-strain-confined synthesis of amorphous TiO_2 mesoporous nanosheets with stable pseudocapacitive lithium storage, Chem. Eng. J. 420 (2021) 129894.
[12] S. Chen, L.-W. Wang, Thermodynamic oxidation and reduction potentials of photocatalytic semiconductors in aqueous solution, Chem. Mater. 24 (18) (2012) 3659–3666.
[13] R. van de Krol and M. Grätzel, Photoelectrochemical Hydrogen Production. Electronic Materials: Science & Technology, Springer US, 2011.
[14] J. Schmidt, W. Vogelsberger, Dissolution kinetics of titanium dioxide nanoparticles: the observation of an unusual kinetic size effect, J. Phys. Chem. B 110 (9) (2006) 3955–3963.
[15] F. Nandjou, S. Haussener, Degradation in photoelectrochemical devices: review with an illustrative case study, J. Phys. D. Appl. Phys. 50 (12) (2017) 124002.
[16] D. Bae, S. Shayestehaminzadeh, E.B. Thorsteinsson, T. Pedersen, O. Hansen, B. Seger, P.C.K. Vesborg, S. Ólafsson, I. Chorkendorff, Protection of Si photocathode using TiO_2 deposited by high power impulse magnetron sputtering for H_2 evolution in alkaline media, Sol. Energy Mater. Sol. Cells 144 (2016) 758–765.
[17] P. Buabthong, J.M. Evans, K.Z. Rinaldi, K.M. Kennedy, H.J. Fu, Z.P. Ifkovits, T.-J. Kuo, B.S. Brunschwig, N.S. Lewis, GaAs microisland anodes protected by amorphous TiO_2 films mitigate corrosion spreading during water oxidation in alkaline electrolytes, ACS Energy Lett. 6 (10) (2021) 3709–3714.
[18] L. Palmolahti, H. Ali-Löytty, M. Hannula, J. Saari, W. Wang, A. Tukiainen, K. Lahtonen, M. Valden, Pinhole-resistant nanocrystalline rutile TiO_2 photoelectrode coatings, Acta Mater. 239 (2022) 118257.
[19] P. Buabthong, Z.P. Ifkovits, P.A. Kempler, Y. Chen, P.D. Nunez, B.S. Brunschwig, K. M. Papadantonakis, N.S. Lewis, Failure modes of protection layers produced by atomic layer deposition of amorphous TiO_2 on GaAs anodes, Energy Environ. Sci. 13 (11) (2020) 4269–4279.
[20] Z. Weng, H. Guo, X. Liu, S. Wu, K. Yeung, P.K. Chu, Nanostructured TiO_2 for energy conversion and storage, RSC Adv. 3 (47) (2013) 24758–24775.
[21] D. Wang, T. Hu, L. Hu, B. Yu, Y. Xia, F. Zhou, W. Liu, Microstructured arrays of TiO_2 nanotubes for improved photo-electrocatalysis and mechanical stability, Adv. Funct. Mater. 19 (12) (2009) 1930–1938.
[22] V. Miikkulainen, M. Leskelä, M. Ritala, R.L. Puurunen, Crystallinity of inorganic films grown by atomic layer deposition: overview and general trends, J. Appl. Phys. 113 (2013) 021301.
[23] Y. Djaoued, S. Badilescu, P.V. Ashrit, D. Bersani, P.P. Lottici, R. Brüning, Low temperature sol-gel preparation of nanocrystalline TiO_2 thin films, J. Sol-Gel Sci. Technol. 24 (2002) 247–254.
[24] S. Abdullah, M. Sahdan, N. Nafarizal, H. Saim, Z. Embong, C.C. Rohaida, F. Adriyanto, Influence of substrate annealing on inducing Ti^{3+} and oxygen vacancy in TiO_2 thin films deposited via RF magnetron sputtering, Appl. Surf. Sci. 462 (2018) 575–582.
[25] M. Hannula, H. Ali-Löytty, K. Lahtonen, E. Sarlin, J. Saari, M. Valden, Improved stability of atomic layer deposited amorphous TiO_2 photoelectrode coatings by thermally induced oxygen defects, Chem. Mater. 30 (4) (2018) 1199–1208.
[26] H. Ali-Löytty, M. Hannula, J. Saari, L. Palmolahti, B.D. Bhuskute, R. Ulkuniemi, T. Nyyssönen, K. Lahtonen, M. Valden, Diversity of TiO_2: controlling the molecular and electronic structure of atomiclayer-deposited black TiO_2, ACS Appl. Mater. Interfaces 11 (3) (2019) 2758–2762.
[27] L. Palmolahti, H. Ali-Löytty, M. Hannula, T. Tinus, K. Lehtola, A. Tukiainen, J. Reuna, M. Valden, Mixed phase Ti^{3+}-rich TiO_2 thin films by oxide defect engineered crystallization, accepted for publication in Nanoscale, 2024.
[28] W.-H. Cheng, M.H. Richter, M.M. May, J. Ohlmann, D. Lackner, F. Dimroth, T. Hannappel, H.A. Atwater, H.-J. Lewerenz, Monolithic photoelectrochemical device for direct water splitting with 19% efficiency, ACS Energy Lett. 3 (8) (2018) 1795–1800.
[29] N. Fairley, V. Fernandez, M. Richard-Plouet, C. Guillot-Deudon, J. Walton, E. Smith, D. Flahaut, M. Greiner, M. Biesinger, S. Tougaard, D. Morgan, J. Baltrusaitis, Systematic and collaborative approach to problem solving using X-ray photoelectron spectroscopy, Appl. Surf. Sci. Adv. 5 (2021) 100112.
[30] D.E. Aspnes, A. Studna, Dielectric functions and optical parameters of Si, Ge, GaP, GaAs, GaSb, InP, InAs, and InSb from 1.5 to 6.0 eV, Phys. Rev. B 27 (2) (1983) 985.
[31] M.A. Green, Self-consistent optical parameters of intrinsic silicon at 300 K including temperature coefficients, Sol. Energy Mater. Sol. Cells 92 (11) (2008) 1305–1310.
[32] M. Wark, J. Tschirch, O. Bartels, D. Bahnemann, J. Rathouskỳ, Photocatalytic activity of hydrophobized mesoporous thin films of TiO_2, Microporous Mesoporous Mater. 84 (1–3) (2005) 247–253.
[33] S.-i. Tanaka, M. Aonuma, N. Hirose, T. Tanaki, The preparation of porous TiO_2 by immersing Ti in NaOH solution, J. Electrochem. Soc. 149 (11) (2002) D167–D171.
[34] Y. Yan, W. Shi, Z. Yuan, S. He, D. Li, Q. Meng, H. Ji, C. Chen, W. Ma, J. Zhao, The formation of Ti–H species at interface is lethal to the efficiency of TiO_2-based dye-sensitized devices, J. Am. Chem. Soc. 139 (5) (2017) 2083–2089.

[35] E. Zhou, L. Tian, Z. Cheng, C. Fu, Design of NiO flakes@$CoMoO_4$ nanosheets core-shell architecture on Ni foam for high-performance supercapacitors, Nanoscale Res. Lett. 14 (2019) 1–11.
[36] C. Powell, A. Jablonski, Surface sensitivity of X-ray photoelectron spectroscopy, Nucl. Instrum. Methods Phys. Res., Sect. A 601 (12) (2009) 54–65.
[37] J. Chastain, R.C. King Jr.. Handbook of x-ray photoelectron spectroscopy, Perkin-Elmer Corporation, 1992.
[38] J.H. Scofield, Hartree-slater subshell photoionization cross-sections at 1254 and 1487 eV, J. Electron Spectrosc. Relat. Phenom. 8 (2) (1976) 129–137.
[39] P. Akhter, A. Baig, A. Mufti, Dissolution of Si (100) layers in NaOH aqueous solutions, J. Phys. D. Appl. Phys. 22 (12) (1989) 1924.
[40] M. Grätzel, Mesoporous oxide junctions and nanostructured solar cells, Curr. Opin. Colloid Interface Sci. 4 (4) (1999) 314–321.
[41] A.R. Bredar, A.L. Chown, A.R. Burton, B.H. Farnum, Electrochemical impedance spectroscopy of metal oxide electrodes for energy applications, ACS Appl. Energy Mater. 3 (1) (2020) 66–98.
[42] N. Baram, Y. Ein-Eli, Electrochemical impedance spectroscopy of porous TiO_2 for photocatalytic applications, J. Phys. Chem. C 114 (21) (2010) 9781–9790.
[43] S. Prabaharan, R. Vimala, Z. Zainal, Nanostructured mesoporous carbon as electrodes for supercapacitors, J. Power Sources 161 (1) (2006) 730–736.
[44] M.-C. Chien, G.-J. Wang, M.-C. Yu, Nanopore size estimation by electrochemical impedance spectroscopy analysis, Jpn. J. Appl. Phys. 47 (9R) (2008) 7459.
[45] J. Saari, H. Ali-Loytty, M.M. Kauppinen, M. Hannula, R. Khan, K. Lahtonen, L. Palmolahti, A. Tukiainen, H. Gronbeck, N.V. Tkachenko, et al., Tunable Ti^{3+}-mediated charge carrier dynamics of atomic layer deposition-grown amorphous TiO_2, J. Phys. Chem. C 126 (9) (2022) 4542–4554.
[46] D. Mergel, D. Buschendorf, S. Eggert, R. Grammes, B. Samset, Density and refractive index of TiO_2 films prepared by reactive evaporation, Thin Solid Films 371 (1–2) (2000) 218–224.
[47] T. Galy, M. Marszewski, S. King, Y. Yan, S.H. Tolbert, L. Pilon, Comparing methods for measuring thickness, refractive index, and porosity of mesoporous thin films, Microporous Mesoporous Mater. 291 (2020) 109677.
[48] A.N. Bashkatov, E.A. Genina, Water refractive index in dependence on temperature and wavelength: A simple approximation, in: Saratov Fall Meeting 2002: Optical Technologies in Biophysics and Medicine IV vol. 5068, SPIE, 2003, pp. 393–395.
[49] N.C. Lindquist, P. Nagpal, K.M. McPeak, D.J. Norris, S.-H. Oh, Engineering metallic nanostructures for plasmonics and nanophotonics, Rep. Prog. Phys. 75 (3) (2012) 036501.